Performance Characteristics of the 3-D OSEM Algorithm in the Reconstruction of Small Animal PET Images

Rutao Yao, Jürgen Seidel, Calvin A. Johnson, *Member, IEEE*, Margaret E. Daube-Witherspoon, *Member, IEEE*,
Michael V. Green, and Richard E. Carson*, *Member, IEEE*

***Abstract*—Rat brain images acquired with a small animal positron emission tomography (PET) camera and reconstructed with the three-dimensional (3-D) ordered-subsets expectation-maximization (OSEM) algorithm with resolution recovery have better quality when the brain is imaged by itself than when inside the head with surrounding background activity. The purpose of this study was to characterize the dependence of this effect on the level of background activity, attenuation, and scatter. Monte Carlo simulations of the imaging system were performed. The coefficient of variation from replicate images, full-width at half-maximum (FWHM) from point sources and image profile fitting, and image contrast and uniformity were used to evaluate algorithm performance. A rat head with the typical levels of five and ten times the brain activity in the surrounding background requires additional iterations to achieve the same resolution as the brain-only case at a cost of 24% and 64% additional noise, respectively. For the same phantoms, object scatter reduced contrast by 3%–5%. However, attenuation degraded resolution by 0.2 mm and was responsible for up to 12% nonuniformity in the brain images suggesting that attenuation correction is useful. Given the effects of emission and attenuation distribution on both resolution and noise, simulations or phantom studies should be used for each imaging situation to select the appropriate number of OSEM iterations to achieve the desired resolution–noise levels.**

***Index Terms*—Ordered-subsets expectation-maximization (OSEM) algorithm, reconstruction, small animal PET imaging, three-dimensional (3-D) volume imaging.**

I. INTRODUCTION

DEDICATED small animal positron emission tomography (PET) scanners [1]–[3] offer the possibility of a wide range of *in vivo* studies including the study of unique animal models of human diseases [4]–[6]. In order to perform quantitative analysis of tracers in rats and mice, the highest possible spatial resolution is desirable for these systems. While resolution recovery algorithms can improve image resolution, the cost is increased noise [7], [8]. This can be offset by higher system sensitivity, which is available with the development of three-dimensional (3-D) acquisition and reconstruction methods [2], [9], [10].

For a 3-D small animal PET scanner with very fine (0.2-mm) spatial sampling [11], the computational burden of reconstruction is substantial. A parallelized version of the ordered-subsets expectation-maximization (OSEM) algorithm [12] has been implemented [13] on an IBM SP2 parallel computer. The 3-D OSEM algorithm was previously shown to improve image quality [13] compared with the 3-D reprojection method [14], achieving resolution better than 1 mm for this camera. However, in our subsequent applications to *in vivo* rat brain data, the OSEM images did not appear to achieve the same resolution, i.e., small brain structures were not clearly delineated. Furthermore, we observed that image quality was significantly better when the brain was imaged by itself than when the brain was inside the head with surrounding background activity. Since *in vivo* brain images must be obtained within an intact head, the impact of factors emanating from the presence of the head, i.e., background activity, scatter, and attenuation, must be assessed to understand the behavior of the reconstruction algorithm and to optimize the final image.

The performance of maximum-likelihood (ML) iterative reconstruction algorithms has been evaluated extensively [7], [15]–[17]. For human scanners, the reconstruction kernel, the choice of postprocessing sieve, the number of iterations and the object size influence the quality of the reconstructed image. There are, however, a number of differences between human-sized and small-animal 3-D cameras. Given the very small structure sizes, the highest possible resolution is necessary for animal imaging. However, without radiation dose limits, higher statistical quality can often be achieved (if specific activity is not a limit), allowing the possibility of resolution recovery. Because of the very fine spatial sampling, acquisitions of even a few million counts may have an average count per projection line of less than 1, so that the Poisson characteristics of the data become more important. The axial acceptance angle of small-animal 3-D cameras is also typically larger than that of human-sized scanners and the smaller size of the animal also produces less attenuation and scatter. All of these differences will be reflected quantitatively and qualitatively in the reconstructed images. Therefore, it is important to evaluate these factors for the rat brain imaging situation of interest here in order to more effectively perform reconstructions.

Manuscript received June 10, 1999; revised June 17, 2000. The Associate Editor responsible for coordinating the review of this paper and recommending its publication was D. Townsend. *Asterisk indicates corresponding author*.

R. Yao and *R. E. Carson are with the PET Department, National Institutes of Health, Bethesda, MD 20892 USA.

J. Seidel and M. V. Green are with the Nuclear Medicine Department, National Institutes of Health, Bethesda, MD 20892 USA.

C. A. Johnson is with the Center for Information Technology, National Institutes of Health, Bethesda, MD 20892 USA.

M. E. Daube-Witherspoon is with the Department of Radiology, University of Pennsylvania, Philadelphia, PA 19104 USA.

Publisher Item Identifier S 0278-0062(00)07996-9.

The objective of this study is to assess quantitatively the effects of surrounding background activity, attenuation, and scatter for a very high spatial resolution ($<$1 mm) camera. In order to control these effects, several mathematical phantoms were designed and Monte Carlo simulations of an existing imaging system were performed to produce data sets where these factors could be controlled through the simulation process. In addition, measured rat brain data were artificially merged into simulated data to assess the impact of background activity in the brain images. Images were evaluated using noise, resolution, contrast, and homogeneity indexes calculated from the reconstructed images.

II. METHODS

A. Existing PET Scanner

The small-animal PET system used in this work consists of two opposing 4-mm-thick slab NaI(Tl) position-sensitive photomultiplier tube (PSPMT) cameras [11], [13], each with an effective area of 50 × 50 mm and separated by 128 mm. The PSPMTs provide a continuous x–y read-out that is sampled onto 0.195-mm-square detection bins (256 × 256 sampling array). The detectors are stationary; the object is rotated at least 360° during acquisition to obtain a complete data set. At the center of the field of view, each camera has an intrinsic point spread function (PSF) with full-width at half-maximum (FWHM) of 1.0 mm, and a coincidence PSF with a FWHM of 1.2 mm [11], [18]. Acquired data were recorded in list-mode.

B. Monte Carlo Simulation

PET acquisitions were simulated using a Monte Carlo program specifically designed for this camera that modeled ^{18}F positron range, depth of interaction effects, scintillation crystal scatter, redundant sampling, and spatial variation in detector sensitivity. Random coincidences and spatial resolution nonuniformities were not included. With the photoelectric events and scatter in both the object and the detector included, the recorded events were tagged with their history of interactions. Therefore, it was possible to distinguish scattered and nonscattered events in the acquired data. Scatter within the detector comprises a significant fraction of the acquired events (56%), so this effect was included in the reconstruction kernel. In this work, only object scatter was studied. Hereafter, the term scatter means specifically object scatter.

C. Mathematical Phantoms

Mathematical phantoms (Fig. 1) were designed to imitate the situation when the rat brain is imaged by itself [Fig. 1(a)] and when the brain is in the rat head with varying amounts of activity within the surrounding rat head volume [Fig. 1(b) and (c)]. A uniform attenuation medium (μ = 0.0096 mm^{-1}) was used for all the phantoms in this study.

1) Rat Brain Only [Fig. 1(a)]: The design of the rat brain simulation was based on measured head images. A cylinder of 16 mm diameter, 20 mm height was used to represent the brain. Two identical small hot cylinders with diameter of 3.2 mm and length of 10 mm were inserted in the brain portion to simulate localized neuroreceptor uptake (see Section II-D). Three point sources were placed in the same plane near the center of the brain to measure spatial resolution. The relative activity concentrations in rat brain, cylinders and point sources were 1 : 4 : 50.

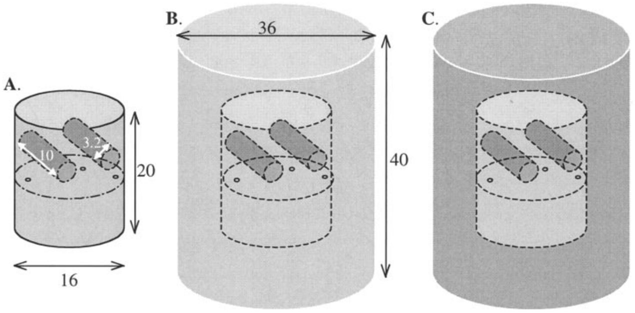

Fig. 1. Three mathematical phantoms for simulating (a) the rat brain only, (b) rat brain with low background, and (c) rat brain with high background. The two small cylinders emulate neuroreceptor uptake and are used as hot VOIs for noise and contrast evaluations. The point sources were used for resolution measurement. All dimensions are in mm. The rotation axis of the scanner is vertical. The axis of the brain and head cylinders is parallel to the axis of rotation. The 3.2-mm diameter cylinders have their primary axis aligned along the transverse slices.

2) Rat Brain with Low Background [Fig. 1(b)]: The rat brain phantom of Fig. 1(a) was placed in a larger cylinder of 36-mm diameter and 40-mm height filled with an activity concentration equal to that in the brain. The total activity in the outside cylinder was five times that in the brain area.

3) Rat Brain with High Background [Fig. 1(c)]: The distribution was the same as the previous phantom except that the activity concentration in the rat head surrounding the brain was twice that in the brain.

D. Measured Brain with Artificial Background Activity

To assess the impact of background activity on rat brain image quality, a measured rat brain data set was combined with simulated surrounding background activity. A rat was injected with 222 MBq (6 mCi) of [^{18}F]FCWAY, a ligand that binds selectively to 5-HT$_{1A}$ receptors [19]. At 30 min postinjection, the rat was sacrificed and the brain was excised from the head. The brain was mounted in the scanner and was scanned for 3 h using three full revolutions. The total activity in the brain at the start of scanning was 0.74 Mbq (20 μCi) resulting in singles rates less than 10 000 s^{-1} and a negligible randoms fraction of <0.01%. Correction factors for redundant sampling of lines of response and radioactive decay were calculated and the measured data were corrected.

Brain voxels were defined by applying a connectivity and threshold segmentation algorithm to a preliminary OSEM rat brain image. By eliminating these voxels from the head-cylinder [the outermost cylinder in Fig. 1(b) and (c)], a brain-shaped void (4266 mm^3) was created within the cylinder. The cylinder volume outside this void was filled with uniform activity and list-mode data were simulated (without radioactive decay) and concatenated to the measured rat brain data to generate a new data set for the case of imaging a rat brain with a surrounding head. Note that the corrected rat brain data are no longer Poisson distributed and systematic errors in the reconstructions could be

TABLE I
SUMMARY OF EXPERIMENTS

Object	Simulated effects	Replicates	Brain only	Brain with low back-ground	Brain with high back-ground	Evaluation indices
			Total counts (millions)			
Simulated brain	No attenuation or scatter	20	0.3	1.8	3.4	Resolution and noise
	No attenuation or scatter	1	6.5	36.5	66.5	Resolution. uniformity, and contrast
	Attenuation only	1	5.7	26.3	49.6	Resolution. uniformity, and contrast
	Attenuation and scatter	1	5.9	28.2	54.0	Resolution. uniformity, and contrast
Measured rat brain embedded in simulated background	No attenuation or scatter	1	0.7	4.9	7.8	Visual assessment

All datasets were reconstructed up to 300 iterations.

produced. However, such effects would be expected to be similar for reconstructed images with and without simulated background activity and should, therefore, have little effect on the qualitative comparison between these images.

E. Simulations

A summary of all the experiments is presented in Table I.

1) Surrounding Background Activity: Acquisitions with totals of 6.5, 36.5, and 66.5 million counts were generated for the brain, brain with low background, and brain with high background mathematical phantoms, respectively. Photon interactions within the object were disabled in the Monte Carlo simulation so there were no scatter or attenuation effects in these simulated data. The full data sets were reconstructed to produce high-statistics images for the purpose of measuring spatial resolution. To estimate noise, twenty replicate acquisitions were extracted from each of these three acquisitions by randomly assigning 1/20th of the total events to each replicate, resulting in total counts of 0.3, 1.8, and 3.4 million counts per replicate.

2) Measured Brain Embedded in Simulated Background: The total number of counts acquired in the rat $[^{18}F]$FCWAY brain measurement was 0.72 million. Acquisitions for the uniform head background activity were simulated without attenuation or scatter and with total counts of six and ten times that in the measured brain. These factors are typical of our observations with actual rat data.

3) Attenuation and Scatter: With both attenuation and scatter effects enabled, acquisitions were simulated for the three mathematical phantoms (Fig. 1). By removing the events tagged as object-scattered, data sets exhibiting only attenuation were also obtained. Scattered events comprised 2%, 7%, and 8% of the total measured events for the brain, brain with low background, and brain with high background phantoms, respectively. Attenuation reduced the counts in the three phantoms by 12%, 28%, and 25%, respectively.

F. Reconstruction

Images were reconstructed using a parallelized 3-D OSEM algorithm on an IBM SP2 parallel computer [13], [20]. Five subsets were used in all reconstructions (for consistency with previous studies) and images up to 60 OSEM iterations, equivalent to 300 EM iterations, were obtained. All references to iteration numbers in this text are EM-equivalent iteration number. The computation time depends on the total counts of the acquired data and the number of processors used [21] and ranged from 0.2 to 3 min/iteration (the total computation time for all reconstructions was ~450 h). A system intrinsic coincidence resolution model (Gaussian function with 1.2-mm FWHM and truncated tails at 5% of maximum value) was incorporated in the system matrix of the algorithm for resolution recovery. Coincidences corresponding to axial angles greater than $\pm 15.2°$ (~8% of total possible projection lines) were not included to reduce computation time. The 3-D reconstructed object consists of $128 \times 128 \times 85$ voxels, which were resliced to $128 \times 128 \times 128$ cubic voxels ($0.39 \times 0.39 \times 0.39$ mm) when image analysis requires volume-matching between phantom and image. No image postsmoothing was performed.

G. Evaluation Indexes

In this work, we only evaluated transverse resolution. Resolution in the axial direction was not measured based on the similarity of axial and transverse resolutions found in previous studies [13]. Since the performance of EM-based algorithms is object-dependent [15], image resolution was calculated in two ways.

1) *Point Source Fitting*: The reconstructed point source image data (nonreplicate data) were fit to a 2-D Gaussian function with five parameters: amplitude, center position in x and y directions, FWHM, and local background. An 11×11 image matrix centered at the point source position was used in the fitting and the typical uncertainty of the FWHM estimate was ~3%. The point source at 2 mm from the center was used for the results presented. The other two sources were ~2 mm from the edge of the brain, so that the Gaussian fitting procedure failed at early iterations when resolution was coarse.

2) *Profile Fitting*: The nine transverse slices intersecting the two small cylinders (3.6 mm thick) were extracted from the phantoms in Fig. 1 and their reconstructed images were summed in the axial direction. Then 21 profiles which were perpendicular to and intersected the axes of the small cylinders were determined. These profiles were fitted individually to the corresponding true phantom profiles convolved with a 1-D Gaussian function with five floating parameters, as above. The typical uncertainty of the FWHM estimate from each profile was ~10%, so to suppress noise, the FWHM values were averaged. The summation over the axial direction was to ensure that axial resolution effects were excluded. The 1-D profile fitting procedure was validated by blurring the true phantom data with 2-D Gaussians (0.8–1.5 mm FWHM) followed by the 1-D profile fitting and the estimated FWHM values were within $1.7 \pm 1.8\%$ of the true values.

Two volumes of interest (VOIs) were defined in the brain region: the *cylinder* VOI was placed in the two small hot cylinders in Fig. 1 and the *brain* VOI was placed in the warm background region of the brain, excluding all voxels within 2.4 mm of the edges of the cylinders and the point sources. The same VOIs were used for all phantoms. To measure image noise, standard deviation (SD) and mean images were calculated from the reconstructed replicate images and the coefficient of variation

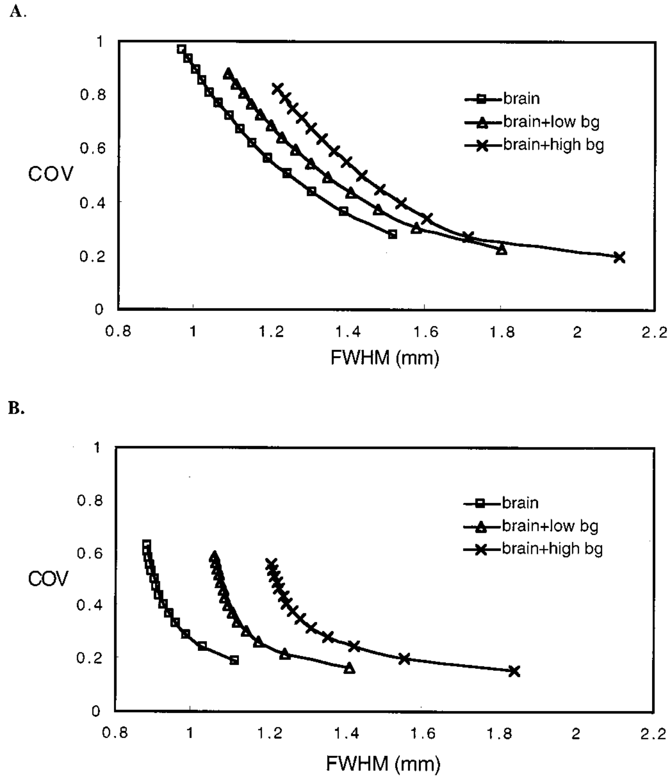

Fig. 2. Noise (COV) of replicate data versus resolution (FWHM) for the three phantoms in Fig. 1. Iterations were from 40 (bottom right) to 300 (upper left) with step size of 20. (a) Data were derived from the *brain* VOI and 2-D Gaussian fitting of the point sources to obtain COV and FWHM, respectively. (b) COV data taken from *cylinder* VOIs and the FWHM values calculated from the profile fitting procedure.

(COV) was calculated in each VOI as the ratio of the average voxel SD to the mean. To assess the effects of attenuation on image uniformity in the brain, the COV within the brain background was calculated from the high-count nonreplicate data. To reduce noise in this calculation, 11 cubes of 125 voxels each were randomly selected from the warm *brain* VOI with the distance between any two cubes larger than four voxels. The mean of each cube (μ_i) was calculated, and the COV of the cube means $(\mathrm{SD}(\mu_i)/\mathrm{mean}(\mu_i))$ was determined for each phantom. The magnitude of nonuniformity introduced by attenuation was calculated by $(\mathrm{COV}^2_{\mathrm{atten}} - \mathrm{COV}^2_{\mathrm{no\_atten}})^{0.5}$. To assess scatter effects, image contrast was calculated as the difference of the mean values in the hot *cylinder* and warm *brain* VOIs divided by the sum of their mean values.

III. RESULTS

A. Background Effects on Noise and Resolution

Fig. 2(a) shows the relationship between resolution (as defined by FWHM from point sources) and image noise (COV in *brain* VOI) as a function of iteration for the three phantoms without scatter or attenuation effects included. As previously reported, resolution improves and noise increases with increasing iterations. The figure demonstrates that increased background activity degrades the resolution of the reconstructed images, i.e., at a fixed iteration, the three phantoms show resolution is degraded by ~0.13 mm as the background activity increases from zero to five and from five to ten times the total activity in the brain. After ~100 iterations, the noise-resolution curves become roughly parallel. By fitting the portions of the curves above 100 iterations, an empirical function was obtained

$$\mathrm{COV} = k \cdot \mathrm{FWHM}^{-\alpha}$$

where α = 2.68 ± 0.16 and k is 0.90, 1.10, and 1.47 for the *brain* VOI of Fig. 1(a)–(c) phantoms, respectively. The uncertainty of the k values was ~1%. For the COV data taken from the *cylinder* VOI (data not shown) and using the point source FWHM values, k is 0.58, 0.73, and 0.96 for the three phantoms. The dependence of k on the level of background activity demonstrates the increase in noise with background activity when images are reconstructed to the same resolution level, i.e., more iterations are required when background activity is present. These additional iterations with low or high background activity produce 24% and 64% higher noise, respectively. This is equivalent to requiring 54% and 169% more counts to achieve the same image quality as in the brain-only case.

As in Fig. 2(a), Fig. 2(b) shows the noise-resolution relationship with the resolution data obtained from profile fitting and the noise (COV) calculated from the *cylinder* VOI. At a given iteration, the profile resolution is from 0.03 to 0.4 mm better than that obtained by fitting the point source data with a Gaussian function, with smaller differences at higher iterations. Compared to the point sources, resolution convergence is faster at early iterations and slower at high iterations. The brain phantom resolution in Fig. 2(b) is 1.1 mm at iteration 40 and improved by ~0.2 mm by iteration 300, whereas in Fig. 2(a), the resolution was 1.5 mm at iteration 40 and improved by 0.55 mm by iteration 300. Fitting the curves in Fig. 2(b) with a geometric function failed, indicating that the noise-resolution relationship in this case follows a different pattern. It is not at all clear that increasing iterations for the low and high background cases will indeed achieve the highest resolution obtained in the brain-only case.

B. Visual Assessment of the Background Effect

Fig. 3(a) shows the coronal rat brain images reconstructed at 40, 100, and 200 iterations from left to right. The bright areas show regions of high 5-HT$_{1\mathrm{A}}$ receptor binding. With increasing iterations, the images become noisier and the contrast between cortical gray matter and internal white matter regions increases, indicating an improvement in resolution. Fig. 3(b) shows one slice of coronal images reconstructed (60 iterations) from the measured rat brain data surrounded by increasing levels of background activity. The counts in the background were 0, 6, and 10 times that in the rat brain. A gradual degradation of resolution from left to right is visible by the change in gray : white contrast, and is consistent with the previous simulation results (Fig. 2). Note that attenuation and scatter effects were not included in the simulated background and these effects would be expected to degrade resolution even further (see Section III-C).

C. Attenuation and Scatter Effects

The effects of attenuation and scatter for the three mathematical phantoms were evaluated using resolution (FWHM from point source), nonuniformity (COV), and contrast. With

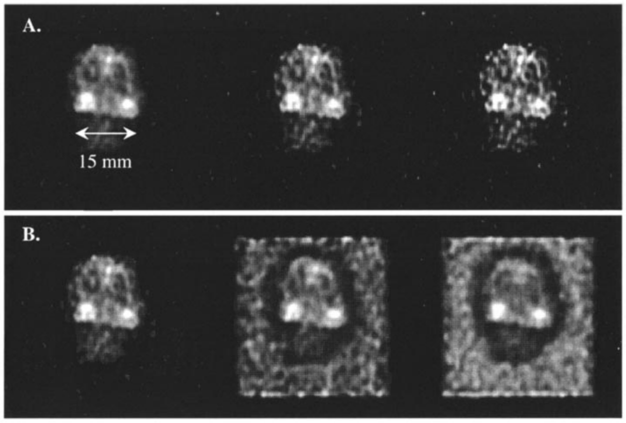

Fig. 3. (a) [^{18}F]FCWAY rat brain images aligned along the coronal plane reconstructed with 40, 100, and 200 OSEM iterations. The horizontal width of the brain is ~15 mm. (b) From left to right, the total background activity in the images is 0, 6, and 10 times the activity in the brain, respectively. Sixty iterations were used for these three images. The images in each row were scaled to the maximum value of the left image.

or without background activity, attenuation slows resolution convergence. By 50 iterations, the FWHM of the no-attenuation case was ~0.2 mm better than the attenuation case, for the three mathematical phantoms (Fig. 1). This resolution difference persisted uniformly for subsequent iterations. With five and ten times activity in the background, the brain nonuniformity (COV) introduced by attenuation was 5.2% and 11.6%, respectively. Thus, even with the same attenuation object, the brain nonuniformity was larger with more activity outside the brain.

The impact of scattered events is small with this camera geometry. The degradation of resolution due to scatter is less than 0.03 mm and there were minimal effects on nonuniformity compared to the attenuation-only case. Object scatter reduced contrast between the hot *cylinder* and warm *brain* VOIs by 0.2%, 3.1%, and 5.3% for the three phantoms simulated compared to images with only attenuation in the simulation. These results suggest that the effects of scatter in a rat head have a small impact on the final image.

IV. DISCUSSION

A. The Effects of Background Activity on Reconstructed Images

The primary issue in this study is the effect of additional background activity around the object of interest. While this issue is not generally addressed in conventional PET imaging, there is a significant literature to predict the effect of background activity in 2-D imaging. The relationship between noise in a target region and the total object activity has been modeled by Budinger *et al.* [22] and shows that increased total activity produces increased object noise. For filtered backprojection (FBP), direct calculation [23], and approximations [24] of image variance show that voxel noise is driven by the total counts in each projection line, so increasing background activity will increase noise. Using a GE Advance scanner, we have conducted several experiments to verify the effect for 3-D imaging with a small cylinder having uniform activity surrounded by varying concentrations of activity in a uniform large cylinder. Twenty replicate acquisitions were acquired and data were reconstructed with FBP and standard corrections. The noise (COV) in the small cylinder was calculated in the reconstructed images and found to increase by 49% and 84% when background activity was five and ten times that in the small cylinder, respectively. Thus, increased noise due to the presence of surrounding background activity is present for FBP 3-D reconstruction.

B. Why Does Background Activity Slow OSEM Convergence?

Our OSEM results show that increased background activity not only brings about more noise in the reconstructed image at matched resolution, but also slows resolution convergence as shown in Fig. 2. With additional iterations, the resolution for a small structure (point source in this study) can be improved, but at the cost of higher noise. Note that the rate of resolution convergence and the number of additional iterations necessary to achieve the desired convergence is highly object-dependent, as seen by comparing Fig. 2(a) and (b).

To understand how the presence of background activity slows resolution convergence, consider the iteration equation of the EM algorithm [25], [26]

$$\lambda_j^{(k+1)} = \frac{\lambda_j^{(k)}}{Q_j} \sum_i \frac{a_{ij} y_i}{\hat{y}_i}$$

where

λ_j source intensity at voxel j;
k iteration number;
Q_j total detection probability of an event emitted from voxel j;
y_i measured data along the ith projection line;
$\hat{y}_i$ expected value along the ith projection line at iteration k;
a_{ij} probability that a pair of photons leaving voxel j is detected on the ith projection line.

As an imaging example, consider a uniform disc of diameter $L+1$ voxels with count intensity of $\lambda = b$, and with a single high-contrast voxel λ_c in the center with activity c. Assume the projection data are noise free. To estimate the convergence rate of λ_c at iteration k, let $\lambda^{(k)} = b$ for all the background voxels (i.e., they have already converged). We assume a simple isotropic system matrix, with the central voxel contributing equally to all projection lines that intersect it (i.e., $a_{ic} = a$ for projections lines i that intersect the central voxel), so that the expected value of those intersecting projection counts can be written as $a(c+Lb)$. Under these assumptions, a rough approximation for the update equation for the central voxel can be shown to be

$$\lambda_c^{(k+1)} = \lambda_c^{(k)} \frac{c+Lb}{\lambda_c^{(k)} + Lb}.$$

So the fractional convergence of this step, i.e., the size of this step as a fraction of the total change that this voxel will undergo to convergence ($\lambda_c^{(\infty)} = c$), is

$$\frac{\lambda_c^{(k+1)} - \lambda_c^{(k)}}{\lambda_c^{(\infty)} - \lambda_c^{(k)}} = \frac{\lambda_c^{(k)}}{\lambda_c^{(k)} + Lb} \cong \frac{1}{1 + \frac{Lb}{c}} \quad \text{near convergence.}$$

Therefore, the larger the background region and the lower the target-to-background contrast (c/b), the slower the convergence of OSEM. The slower convergence incurred by higher background activity or lower contrast requires more iterations to achieve a desired resolution.

The derivation above may explain a small discrepancy found in resolution values in the current simulations and those reported previously in evaluating OSEM and this camera [13]. In the previous study, the concentration ratio of point source to uniform background was $>1000:1$ and the point source resolution reached 0.74 mm at iteration 300 (60 OSEM iterations). Here, for the brain with low background simulation, the point source contrast was $50:1$ and a FWHM of $\sim$1.1 mm was achieved at the same iteration.

C. Measures of Resolution

Excluding detector effects, FBP images are usually considered to produce uniform resolution. Due to the dependence of the convergence of EM-based algorithms on the object being reconstructed, the traditional point source measure for spatial resolution cannot fully describe the resolution behavior of an image. Liow *et al.* [15] proposed using effective local Gaussian resolution and effective global Gaussian resolution which require specially designed object shapes and high statistics data. In this work, 2-D Gaussian fitting of point sources in a warm background was used to measure the resolution performance of very small objects and profile fitting was used to measure the resolution of larger hot objects. The results show different convergence speeds for different sized objects, consistent with previous reports [15] and with the derivation of the previous sections. As shown in Fig. 2, the cylinder resolution converges more quickly at early iterations, so that further iterations predominantly add only noise with minor improvement in resolution. These varied resolutions with different sized objects suggest that an optimal iteration number for OSEM cannot be chosen in general, but rather must be selected on a case-by-case basis, presumably by simulation or phantom analysis.

D. Are Corrections for Attenuation and Scatter Necessary for Small Animal Imaging?

Due to the size of small animals, it could be assumed that attenuation and scatter would have minimal effects on the reconstructed images. However, the results reported here show that the presence of attenuation may degrade resolution by $\sim$0.2 mm, a nonnegligible effect for these resolution-critical systems. The cause of this resolution degradation is not clear, although we speculate that it may be due to the inconsistency of the projection data when attenuation is present but uncorrected. In addition to the resolution degradation, attenuation introduced up to 12% nonuniformity in the brain portion of the image. Thus, attenuation correction should improve both the resolution and uniformity in small animal PET images. In the brain, it is likely that nonuniformities in attenuation coefficient can be ignored, so that an analytical attenuation correction should not be difficult to implement in the system model, given a measurement of the outer edge of the imaging object. Further work is needed to validate this claim.

Scatter may introduce 3%–5% contrast loss with no effect on resolution. Although the highest possible contrast is desirable for high-resolution images, it appears from these data that scatter effects may be ignored in brain studies of small animals.

V. CONCLUSION

Simulations of an existing small-animal PET camera were used to evaluate the characteristics of OSEM images of the rat brain. Attenuation degraded resolution by 0.2 mm for the phantoms simulated and introduced nonuniformity in the images, suggesting that attenuation correction should be performed. Object scatter for a rat-head sized subject had little influence on image characteristics. The primary result is that reconstructions of a rat brain with surrounding background activity levels commonly seen in real imaging situations, i.e., five and ten times the brain activity, require additional iterations to achieve the same resolution as brain-only studies with an increase of 24%–64% in noise. Thus, unlike linear reconstruction algorithms, great care must be taken when specifying the resolution of *in vivo* small animal images reconstructed with resolution recovery algorithms. The object-dependency of resolution and the variation in resolution convergence caused by background activity suggest that simulations or phantom studies should be used for each imaging situation to select the appropriate number of OSEM iterations to achieve the desired resolution. Alternatively, a modified iterative reconstruction algorithm that maintains accurate statistical modeling while providing more uniform resolution convergence may prove more useful than OSEM for high-resolution imaging studies.

ACKNOWLEDGMENT

This study utilized the high-performance computational capabilities of the IBM RISC/6000 SP system at the Center for Information Technology, National Institutes of Health, Bethesda, MD. The authors thank L. Lang and E. Jagoda for their collaboration in the [^{18}F]FCWAY rat study.

REFERENCES

[1] L. Lecomte, J. Cadorette, S. Rodrigue, D. Lapointe, D. Rouleau, M. Bentourkia, R. Yao, and P. Msaki, "Initial results from the Sherbrooke avalanche photodiode positron tomograph," *IEEE Trans. Nucl. Sci.*, vol. 43, pp. 1952–1957, 1996.

[2] S. R. Cherry, Y. Shao, R. W. Silverman, K. Meadors, S. Siegel, A. Chatziioannou, J. W. Young, W. Jones, J. C. Moyers, D. Newport, A. Boutefnouchet, T. H. Farquhar, M. Andreaco, M. J. Paulus, D. M. Binkley, R. Nutt, and M. E. Phelps, "MicroPET: A high resolution PET scanner for imaging small animals," *IEEE Trans. Nucl. Sci.*, vol. 44, pp. 1161–1166, 1997.

[3] P. M. Bloomfield *et al.*, "The design and physical characteristics of a small animal positron emission tomograph," *Phys. Med. Biol.*, vol. 40, pp. 1105–1126, 1995.

[4] C. J. Marriott, J. E. Cadorette, R. Lecomte, V. Scasnar, J. Rousseau, and J. E. van Lier, "High-resolution PET imaging and quantitation of pharmaceutical biodistributions in a small animal using avalanche photodiode detectors," *J. Nucl. Med.*, vol. 35, pp. 1390–1396, 1994.

[5] N. M. Spyrou, J. M. Sharaf, and S. Rajeswaran, "Developments in tomographic methods for biological tracae element research," *Biol. Trace. Elem. Res.*, vol. 43–45, pp. 55–63, 1994.

[6] S. P. Hume and T. Jones, "Positron emission tomography (PET) methodology for small animals and its application in radiopharmaceutical preclinical investigation," *Nucl. Med. Biol.*, vol. 25, pp. 729–732, 1998.

[7] R. E. Carson, Y. Yan, B. Chodkowski, T. K. Yap, and M. E. Daube-Witherspoon, “Precision and accuracy of regional radioactive quantitation using the maximum likelihood EM reconstruction algorithm,” *IEEE Trans. Med. Imag.*, vol. 13, pp. 526–537, 1994.

[8] J. S. Liow and S. C. Strother, “Noise and signal decoupling in maximum likelihood reconstructions and Metz filters for PET images,” in *Proc. 1991 IEEE Nucl. Sci. Symp. Med. Imag. Conf.*, 1992, pp. 901–903.

[9] D. L. Bailey, M. P. Miller, T. J. Spinks, P. M. Bloomfield, L.. Livieratos, H. E. Young, and T. Jones, “Experience with fully 3-D PET and implications for future high-resolution 3D tomographs,” *Phys. Med. Biol.*, vol. 43, pp. 777–786, 1998.

[10] T. H. Farquhar, A. Chatziioannou, and S. R. Cherry, “An evaluation of exact and approximate 3–D reconstruction algorithms for a high-resolution, small-animal PET scanner,” *IEEE Trans. Med. Imag.*, vol. 17, pp. 1073–1080, 1998.

[11] J. Seidel, W. R. Gandler, and M. V.. Green, “A very high resolution single-slice small animal PET scanner based on direct detection of coincidence line endpoints,” *J. Nucl. Med.*, vol. 35, p. 40P, 1994.

[12] H. M. Hudson and R. S. Larkin, “Accelerated image reconstruction using ordered subsets of projection data,” *IEEE Trans. Med. Imag.*, vol. 13, pp. 601–609, 1994.

[13] C. A. Johnson, J. Seidel, R. E. Carson, W. R. Gandler, A. Sofer, M. V. Green, and M. E. Daube-Witherspoon, “Evaluation of 3-D reconstruction algorithms for a small animal PET camera,” *IEEE Trans. Nucl. Sci.*, vol. 44, pp. 1303–1308, 1997.

[14] P. E. Kinahan and J. G. rogers, “Analytic 3D image reconstruction using all detected event,” *IEEE trans. Nucl. Sci.*, vol. 36, pp. 964–968, 1998.

[15] J. S. Liow and S. C. Strother, “The convergence of object dependent resolution in maximum likelihood based tomographic image reconstruction,” *Phys. Med. Biol.*, vol. 38, pp. 55–70, 1993.

[16] J. S. Liow, S. C. Strother, K. Rehm, and D. A. Rottenberg, “Improved resolution for PET volume imaging through three-dimensional iterative reconstruction,” *J. Nucl. Med.*, vol. 38, pp. 1623–1631, 1997.

[17] J. A. Stamos, W. L. rogers, N. H. Clinthorne, and K. F. Koral, “Object-dependent performance comparison of two iterative reconstruction algorithms,” *IEEE Trans. Nucl. Sci.*, vol. 35, pp. 611–614, 1988.

[18] J. Seidel, M. V. Green, and W. R. Gandler, “Estimated spatial resolution of a single slice, small animal PET scanner using position-sensitive photomultiplier tubes for event pair location,” in *Proc. 29th Annu. Meet. Assoc. Adv. Med. Instrum. (AAMI)*, Washington, DC, 1994, p. 85.

[19] L. Lang, E. Jagoda, B. Schmall, B.-K. Vuong, H. R. Adams, D. L. Nelson, R. E. Carson, and W. C. Eckelman, “Development of fluorine-18-labeled 5-HT_{1A} antagonists,” *J. Med. Chem.*, vol. 42, pp. 1576–1586, 1999.

[20] C. A. Johnson, Y. Yan, R. E. Carson, R. L. Martino, and M. E. Daube-Witherspoon, “A system for the 3D reconstruction of retracted-septa PET data using the EM algorithm,” *IEEE Trans. Nucl. Sci.*, vol. 42, pp. 1223–1227, 1994.

[21] C. A. Johnson, *Nonlinear Optimization for Volume PET Reconstruction*. Fairfax, VA: Dept. Oper. Res. Eng., George Mason Univ., 1997.

[22] T. F. Bidinger, S. E. Derenzo, W. L. Greenberg, G. T. Gullberg, and R. H. Huesman, “Quantitative potentials of dynamic emission computed tomography,” *J. Nucl. Med.*, vol. 19, pp. 309–315, 1978.

[23] N. M. Alpert, D. A. Chesler, J. A. Correia, R. H. Ackerman, J. Y. Chang, S. Finklestein, S. M. Davis, G. L. Brownnell, and J. M. Taveras, “Estimation of the local statistical noise in emission computed tomography,” *IEEE Trans. Med. Imag.*, vol. MI-1, pp. 142–146, 1982.

[24] R. E. Carson, Y. Yan, M. E. Daube-Witherspoon, N. Freedman, S. L. Bacharach, and P. Herscovitch, “An approximation formula for the variance of PET region-of-interest values,” *IEEE Trans. Med. Imag.*, vol. 12, pp. 240–250, 1993.

[25] L. A. Shepp and Y. Vardi, “Maximum likelihood reconstruction in positron emission tomography,” *IEEE Trans. Med. Imag.*, vol. MI-1, pp. 113–122, 1982.

[26] K. Lange and R. Carson, “EM reconstruction algorithms for emission and transmission tomography,” *J. Comput. Assist. Tomogr.*, vol. 8, pp. 306–316, 1984.